Active Acoustic Metasurface: Complete Elimination of Grating Lobes for High-Quality Ultrasound Focusing and Controllable Steering

Yaxi Shen,[1,2] Xuefeng Zhu,[2,*] Feiyan Cai,[1,†] Teng Ma,[1,‡] Fei Li,[1] Xiangxiang Xia,[1] Yongchuan Li,[1] Congzhi Wang,[1] and Hairong Zheng[1]

[1]*Paul C. Lauterbur Research Center for Biomedical Imaging, Institute of Biomedical and Health Engineering, Shenzhen Institutes of Advanced Technology, Chinese Academy of Science, Shenzhen 518055, China*

[2]*School of Physics and Innovation Institute, Huazhong University of Science and Technology, Wuhan 430074, China*

Eliminating the grating lobes is significant in ultrasonics. For example, highly efficient ultrasound focus and flexible focus steering without off-target heating for medical applications require the total rejection of grating lobes and side lobes. We investigate analytically, numerically, and experimentally the physical causes of grating lobes in ultrasound beam engineering. We find that the generation of grating lobes is attributed to two main factors, namely, the diffraction from the finite-sized source array and the different phase delays of the phased array. Based on these findings, we design and implement an active acoustic metasurface to completely eliminate the grating lobes. The lab-made metasurface comprises 16×16 square-lattice elements of subwavelength thickness, where each element is a supercell with 4×4 piezoelectric sheets in a matrix of epoxy resin. By tailoring the ratio of the supercell width over the lattice constant, the grating lobes due to the structure diffraction can be completely suppressed. With a programmable multichannel drive, we further impose Gaussian-shaped amplitude modulation on the metasurface to wipe out the grating lobes induced by inhomogeneous phase delays. Our experimental results convincingly demonstrate that the active metasurface with programmable phase and amplitude modulations shows a high performance in grating-lobe-proof and steerable ultrasound focusing.

I. INTRODUCTION

Ultrasound beam engineering is an upcoming field for versatile medical applications. For example, high-intensity focused ultrasound has been used in clinics to instantly destroy tumor cells due to its minimal invasion, high precision, and fewer side effects [1–4]. Recently, focused ultrasound has become a promising tool for noninvasive neural stimulation *in vivo* [5–12]. Early proof-of-concept experiments suggested that ultrasound can modify the perception of tactile sensations [6–8]. Since then, much research has shown that focused ultrasound has therapeutic potential for treating a variety of neurological diseases [9–12]. In ultrasound beam engineering, the commonly used sparse transducer array offers both electrically controlled beam steering and phase-aberration correction for minimizing the focus size [13–20]. However, the projected ultrasound field has many unavoidable grating lobes and side lobes, which may cause harmful physical heating

in nontargeted regions. Thus, it is significant to develop an integrated device to implement highly efficient ultrasound focus as well as freewheeling focus steering without off-target heating, which is useful in medical applications.

In the following, we organize our work into three parts. In the first part, we investigate the ultrasound field pattern from a one-dimensional (1D) source. The diffraction field is found to be closely related to the geometrical parameters of the source. For example, as the source length increases, a higher numerical aperture ensures a smaller FWHM of the main lobe with a greater number of side lobes included. We reveal that after discretizing the line source into small identical elements, numerous unwanted grating lobes will emerge, which can be well suppressed on the condition that the spacing between adjacent elements equals the element length. We also show that the Gaussian-shaped amplitude modulation with a small FWHM at the closely-packed 1D source array perfectly eliminates the grating lobes and side lobes, which can be further extended into two-dimensional (2D) arrays. In the second part, we propose an active acoustic metasurface to verify the theory analysis [21–34]. The integrated metasurface is made of 16×16 square-lattice elements of subwavelength thickness, where

---

*xfzhu@hust.edu.cn
†fy.cai@siat.ac.cn
‡teng.ma@siat.ac.cn

the element is a supercell with 4×4 piezoelectric sheets in a matrix of epoxy resin. For each element, the phase and amplitude of the radiated ultrasound are programmable via a powerful electric multichannel drive. The metasurface operates underwater in the ultrasound regime, which is packaged between a matching layer and a backing layer for practical use. In experiments, we demonstrate high-quality steerable focusing with the grating lobes and side lobes completely eliminated by imposing Gaussian-shaped amplitude modulation on the metasurface. The measured results are in perfect agreement with numerical simulations, confirming the functionality of the state-of-the-art device. In the last part, main conclusions are provided.

II. THEORY

The controlling equation of acoustic wave propagation in free space is [35,36]

$$\nabla^2 p(\mathbf{r}, t) - \frac{1}{c^2} \frac{\partial^2 p(\mathbf{r}, t)}{\partial t^2} = 0, \tag{1}$$

where ∇^2 denotes the Laplace operator, c and $p(\mathbf{r}, t)$ are the speed of sound and the acoustic pressure at position $\mathbf{r}$ and the time t, respectively. The acoustic pressure can be expressed in the form of $p(\mathbf{r}, t) = \text{Re}\{p(\mathbf{r})e^{-j\omega t}\}$, where $p(\mathbf{r})$ is the complex pressure amplitude at position $\mathbf{r}$ and ω is the angular frequency. Substituting this form into Eq. (1), the wave equation is simplified into the Helmholtz equation $(\nabla^2 + k^2)p(\mathbf{r}) = 0$, where k is the wave number. According to Green's theorem, two spatial wave functions $U(r)$ and $G(r)$ satisfy the Helmholtz equation, which can lead to the following Kirchhoff diffraction integral equation [36]

$$U(\mathbf{r}_i) = \frac{1}{4\pi} \int_S \left[G \frac{\partial U(\mathbf{r}_s)}{\partial n} - U(\mathbf{r}_s) \frac{\partial G}{\partial n} \right] dS, \tag{2}$$

where S is an arbitrary closed surface, $\partial/\partial n$ is the normal derivative operator, and $U(\mathbf{r}_i)$ and $U(\mathbf{r}_s)$ are the acoustic pressure fields inside and on the closed surface S, respectively. By setting the wave function $G(r) = e^{jkr}/r$ with r the distance from the surface point $\mathbf{r}_s$ to the inside field point $\mathbf{r}_i$, we will derive the Rayleigh diffraction integral from the Kirchhoff integral

$$U(\mathbf{r}_i) = \frac{1}{j\lambda} \int_\Sigma U(\mathbf{r}_s) \frac{1}{r} e^{jkr} dS, \tag{3}$$

where Σ denotes the integral surface. Here, we consider a simple case of the 1D line source, as shown in Fig. 1(a), with the line source parallel to the x axis and the acoustic wave propagating along the z axis. From Eq. (3), the
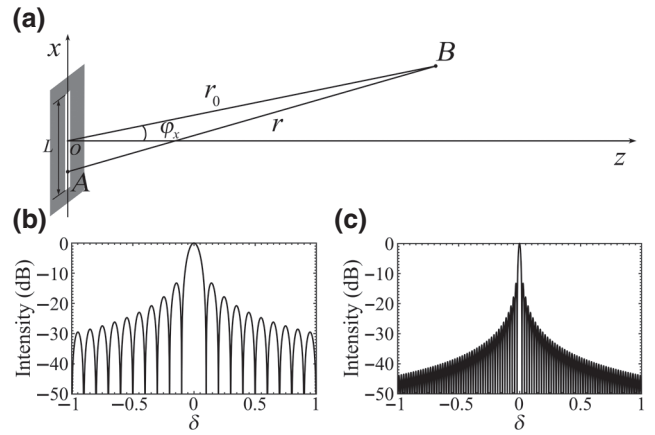

FIG. 1. (a) A schematic of wave diffraction from a 1D line source. (b), (c) The intensity distributions of diffraction fields from the line source, where the source lengths are $L = 10\lambda$ and $L = 50\lambda$, respectively. In (b) and (c), the parameter $\delta = \sin\varphi_x$, with φ_x ranging from $-\pi/2$ to $\pi/2$.

pressure field at a point (r_0, φ_x) is given by

$$p(r_0, \varphi_x) = \frac{1}{j\lambda} \int_l p(x) \frac{1}{r} e^{jkr} dx, \tag{4}$$

where φ_x is the angle between r_0 and the z axis and $r = \sqrt{r_0^2 + x^2 + 2r_0 x \sin\varphi_x}$. With the approximation $r \approx r_0$ in the denominator and $r \approx r_0 + x \sin\varphi_x$ in the exponential term, and by setting $\delta = \sin\varphi_x$, Eq. (4) is reduced to

$$p_{r_0}(\delta) = \frac{1}{j\lambda} \frac{1}{r_0} e^{jkr_0} \int_l p(x) e^{jkx\delta} dx. \tag{5}$$

Equation (5) is actually the Fourier transform of the pressure distribution on the line source $p(x)$. For the boundary conditions of the Kirchhoff diffraction, the pressure is unchanged after ultrasound passes through the diffraction aperture, while the pressure equals zero in other regions. Thus, the pressure waveform $p(x)$ can be expressed by the product of the excitation function $h(x)$ and the aperture function $t(x)$, where the aperture function is determined by the geometry of the source. Therefore, we can separately design $h(x)$ and $t(x)$ to implement specific diffraction fields. Based on the convolution theorem of the Fourier transform, Eq. (5) can be written into [37]

$$p_{r_0}(\delta) = \frac{e^{jkr_0}}{j\lambda r_0} \int_l h(x)t(x)e^{jkx\delta} dx = C_0 \mathcal{F}\{h(x)\} * \mathcal{F}\{t(x)\}, \tag{6}$$

where $C_0 = e^{jkr_0}/j\lambda r_0$, and $\mathcal{F}\{\cdot\}$ and $*$ denote the Fourier transform function and the convolution operator, respectively.

Considering the 1D line source with length L, we set $h(x) = p_0$ and $t(x) = \text{rect}(x/L)$, where $\text{rect}(\cdot)$ is the rectangular function with $\text{rect}(x/L) = 1$ at $|x| \leq L/2$ and $\text{rect}(x/L) = 0$ at $|x| \geq L/2$. Substituting $h(x)$ and $t(x)$ into Eq. (6), we will obtain the radiation pattern of the 1D line source from

$$p_{r_0}^I(\delta) = C_0 \mathcal{F}\left\{p_0 \text{rect}\left(\frac{x}{L}\right)\right\} = p_0 C_0 L \text{sinc}\left(\frac{L\delta}{\lambda}\right), \quad (7)$$

where $\text{sinc}(\cdot)$ denotes the function $\text{sinc}(x) = \sin(\pi x)/\pi x$. Figures 1(b) and 1(c) show the intensity distributions of diffraction fields at $L = 10\lambda$ and $L = 50\lambda$, respectively, with λ the wavelength. From Figs. 1(b) and 1(c), we find that the source length is related to the width of the main lobe and the number of side lobes. As the length increases, the width of the main lobe decreases with more side lobes included.

Then we consider a generalized case in which the line source is discretized into periodic source elements. We first consider a simple case in which the source consists of periodic points spaced by g, as shown in Fig. 2(a). The number of the points $N = L/g$. In Fig. 2(a), the aperture function can be written as $t(x) = g^{-1}\text{comb}(x/g)\text{rect}(x/L)$, where

$$\text{comb}(x) = \sum_{n=-\infty}^{\infty} \delta(x - n),$$

with n an integer and $\delta(\cdot)$ the Dirac function. All point sources have uniform excitation amplitudes, $h(x) = p_0$. Substituting the expressions $h(x)$ and $t(x)$ into Eq. (6), we will obtain the radiation pattern of the periodic point sources from

$$p_{r_0}^{II}(\delta) = p_0 C_0 \mathcal{F}\left\{\frac{1}{g}\text{comb}\left(\frac{x}{g}\right)\text{rect}\left(\frac{x}{L}\right)\right\}$$

$$= p_0 C_0 \mathcal{F}\left\{\text{rect}\left(\frac{x}{L}\right)\right\} * \mathcal{F}\left\{\frac{1}{g}\text{comb}\left(\frac{x}{g}\right)\right\}$$

$$= p_0 C_0 L \text{sinc}\left(\frac{L\delta}{\lambda}\right) * \text{comb}\left(\frac{g\delta}{\lambda}\right). \quad (8)$$

Comparing Eq. (8) with Eq. (7), the radiation pattern induced by periodic point sources $p_{r_0}^{II}(\delta)$ is the convolution between the radiation pattern induced by a line source $p_{r_0}^I(\delta)$ and the comb function $\text{comb}(g\delta/\lambda)$. Based on the periodic property of the comb function, we derive the diffraction angle of all the grating lobes

$$\varphi_x^n = \sin^{-1}(\delta_n) = \sin^{-1}\left(\frac{n\lambda}{g}\right), \quad (9)$$

where n denotes the order of the grating lobes, namely, $n = \pm 1, \pm 2 \dots$. From Eq. (9), we find that the number of grating lobes is determined by the ratio of the wavelength
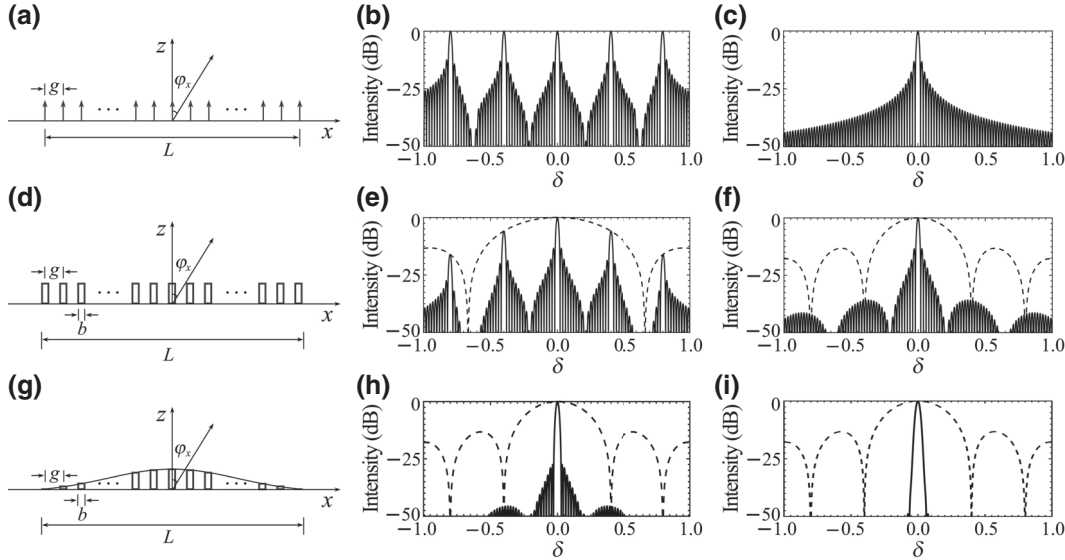

FIG. 2. (a) The 1D source pattern with the pressure field distribution $p(x) = \frac{p_0}{g}\text{comb}\left(\frac{x}{g}\right)\text{rect}\left(\frac{x}{L}\right)$. (b) The intensity distribution of the diffraction field from the source in (a) at $L = 50\lambda$, $g = 2.5\lambda$. (c) The intensity distribution of the diffraction field from the source in (a) at $L = 50\lambda$, $g = 0.9\lambda$. (d) The source pattern with $p(x) = \frac{p_0}{g}\text{comb}\left(\frac{x}{g}\right) \times \text{rect}\left(\frac{x}{L}\right) * \text{rect}\left(\frac{x}{b}\right)$. (e) The intensity distribution of the diffraction field from the source in (d) at $L = 50\lambda$, $g = 2.5\lambda$, $b = 1.5\lambda$. (f) The intensity distribution of the diffraction field from the source in (d) at $L = 50\lambda$, $g = 2.5\lambda$, $b = 2.5\lambda$. (g) The source pattern with $p(x) = \frac{p_0 e^{-x^2/\tau^2}}{g}\text{comb}\left(\frac{x}{g}\right) \times \text{rect}\left(\frac{x}{L}\right) * \text{rect}\left(\frac{x}{b}\right)$. (h) The intensity distribution of the diffraction field from the source in (g) at $L = 50\lambda$, $g = 2.5\lambda$, $b = 2.5\lambda$, $\tau = 20\lambda$. (i) The intensity distribution of the diffraction field from the source in (g) at $L = 50\lambda$, $g = 2.5\lambda$, $b = 2.5\lambda$, $\tau = 13\lambda$.

and the period, that is, λ/g. At the operation frequency, the diffraction angle of the grating lobes will increase as the period g decreases. Figure 2(b) shows the intensity distribution of the diffraction field at $g = 2.5\lambda$ and $L = 50\lambda$. In addition to the main lobe at $\delta_0 = 0$, there exist four grating lobes with diffraction angles of $\varphi_x^{-2} = -53.13°$, $\varphi_x^{-1} = -23.58°$, $\varphi_x^1 = 23.58°$, and $\varphi_x^2 = 53.13°$, which correspond to $\delta_{-2} = -0.8$, $\delta_{-1} = -0.4$, $\delta_1 = 0.4$, and $\delta_2 = 0.8$, respectively. In order to eliminate these grating lobes, one intuitive way is to make the period g smaller than the wavelength λ, as reflected in Eq. (9). For example, in Fig. 2(c), the intensity distribution of the diffraction field at $g = 0.9\lambda$ and $L = 50\lambda$ shows that there exists only the main lobe in the field of view. However, the solution has two disadvantages. First, a smaller period will lead to more source elements, which increases not only the microfabrication difficulty but also the electronic complexity of the multichannel electric drive. Second, many side lobes are still included that give rise to nontrivial off-target heating.

A more practical case is that the periodic source elements have a certain length, as shown in Fig. 2(d). The aperture function thus takes the form of a convolution $t(x) = (1/g)\text{comb}(x/g) \times \text{rect}(x/L) * \text{rect}(x/b)$, with b the length of the source elements. As described in Fig. 2(d), all elements have a uniform excitation amplitude $h(x) = p_0$. Substituting $h(x)$ and $t(x)$ into Eq. (6), we will obtain the radiation pattern of the periodic line sources from

$$p_{r_0}^{III}(\delta) = p_0 C_0 \mathcal{F} \left\{ \frac{1}{g}\text{comb}\left(\frac{x}{g}\right) \times \text{rect}\left(\frac{x}{L}\right) * \text{rect}\left(\frac{x}{b}\right) \right\}$$
$$= p_0 C_0 \mathcal{F} \left\{ \frac{1}{g}\text{comb}\left(\frac{x}{g}\right) \right\} * \mathcal{F} \left\{ \text{rect}\left(\frac{x}{L}\right) \right\} \times \mathcal{F} \left\{ \text{rect}\left(\frac{x}{b}\right) \right\}$$
$$= p_0 C_0 L\text{sinc}\left(\frac{L\delta}{\lambda}\right) * \text{comb}\left(\frac{g\delta}{\lambda}\right) \times b\text{sinc}\left(\frac{b\delta}{\lambda}\right). \quad (10)$$

Comparing Eq. (10) with Eq. (8), the radiation pattern of the periodic line sources $p_{r_0}^{III}(\delta)$ is a product of the radiation pattern of the periodic point sources $p_{r_0}^{II}(\delta)$ and a sinc function $b\text{sinc}(b\delta/\lambda)$. The sinc-type amplitude modulation on the radiation pattern can be employed to effectively reduce the intensity of the grating lobes. For example, in Fig. 2(e), the solid line represents the intensity distribution of the diffraction field at $g = 2.5\lambda$, $L = 50\lambda$, and $b = 1.5\lambda$. The dash line is the function $|b\text{sinc}(b\delta/\lambda)|^2$, which describes the envelope of the intensity curve and shows obvious suppression on the grating lobes. From Eq. (9), the diffraction angles of the grating lobes are $\varphi_x^n = \sin^{-1}(n\lambda/g)$. By setting $b = g$, we obtain the function $\text{sinc}(b\delta/\lambda) = 0$ at those diffraction angles, indicating that all the grating lobes are completely suppressed, as proved in Fig. 2(f), where $g = 2.5\lambda$, $L = 50\lambda$, and $b = 2.5\lambda$. However, in this case, even though the period can be larger with fewer source elements required, there still exist many side lobes that produce off-target heating.

In order to further eliminate the side lobes, we propose to add the Gaussian-shaped modulation in the excitation

function $h(x)$, as shown in Fig. 2(g). In our case, the excitation function can be written into $h(x) = p_0 e^{-x^2/\tau^2}$, where τ denotes the strength of amplitude modulation. Substituting $h(x)$ and $t(x)$ into Eq. (6), we will obtain the radiation pattern of the periodic line sources with Gaussian-modulated excitation amplitudes from

$$p_{r_0}^{IV}(\delta) = C_0 \mathcal{F}\{p_0 e^{-x^2/\tau^2}\}$$
$$* \mathcal{F} \left\{ \frac{1}{g}\text{comb}\left(\frac{x}{g}\right) \times \text{rect}\left(\frac{x}{L}\right) * \text{rect}\left(\frac{x}{b}\right) \right\}$$
$$= \mathcal{F}\{e^{-x^2/\tau^2}\} * p_{r_0}^{III}(\delta)$$
$$= \tau\sqrt{\pi} e^{-\pi^2\tau^2\delta^2/\lambda^2} * p_{r_0}^{III}(\delta). \quad (11)$$

The solid lines in Figs. 2(h) and 2(i) describe the intensity distributions of the diffraction fields at $\tau = 20\lambda$ and $\tau = 13\lambda$, respectively, where the element period $g = 2.5\lambda$, the array size $L = 50\lambda$, and the element length $b = 2.5\lambda$. The results clearly show that the Gaussian-shaped modulation can well suppress the side lobes. As the modulation strength τ decreases below a threshold (the threshold is 13.2λ when $L = 50\lambda$), we only observe the main lobe in the field of view, with grating lobes and side lobes completely eliminated, as shown in Fig. 2(i).

III. RESULTS AND DISCUSSIONS

In this section, we extend our approach into the more useful 2D cases for the experimental demonstration. The diffraction field from the 2D source plane can be written as

$$p_{r_0}(\delta_x, \delta_y) = C_1 \prod_{\alpha=x,y} \mathcal{F}\{h(\alpha)\} * \mathcal{F}\{t(\alpha)\}, \quad (12)$$

where C_1 is the normalization coefficient. Figures 3(a)−3(c) show the intensity distributions of the diffraction fields from three different types of 2D planar sources. Each source consists of square-latticed finite elements. In Fig. 3(a), where $g_\alpha = 2.5\lambda$, $L_\alpha = 50\lambda$, and $b_\alpha = 1.5\lambda$, we find that besides the main lobe in the center, there are many grating lobes together with side lobes in the field of view. In Fig. 3(b), where $g_\alpha = 2.5\lambda$, $L_\alpha = 50\lambda$, and $b_\alpha = 2.5\lambda$, the result reveals that all grating lobes are eliminated, but there still exist obvious side lobes in the x and y directions. In Fig. 3(c), where $g_\alpha = 2.5\lambda$, $L_\alpha = 50\lambda$, $b_\alpha = 2.5\lambda$, and $\tau_\alpha = 13\lambda$, we find that only the main lobe is observed in the field of view with the grating lobes and side lobes completely erased, in agreement with the above discussion in 1D cases.

Based on the theoretical analysis and numerical simulation, we design an active acoustic metasurface for the experimental demonstration. The metasurface comprises 16×16 square-lattice elements with a thickness of about half the wavelength. Each element is a supercell with 4×4
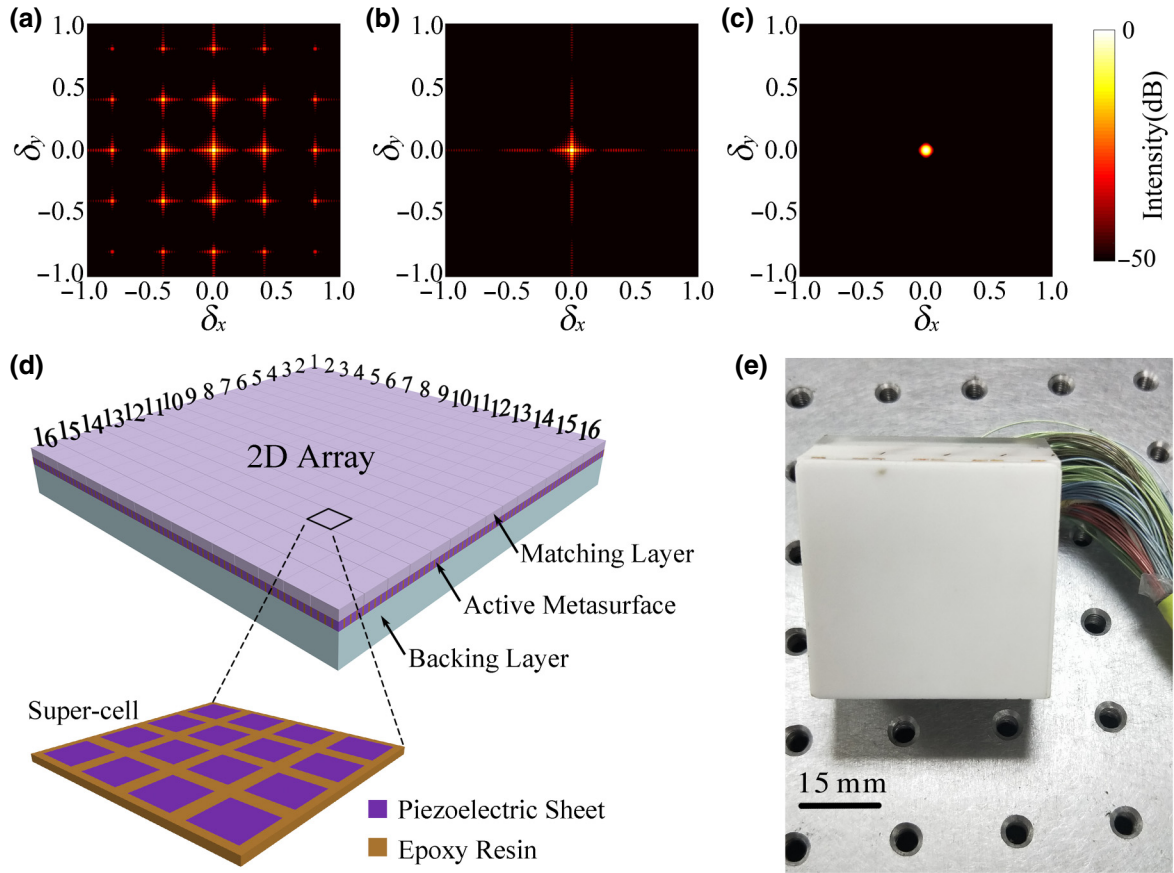
FIG. 3. (a) The intensity distribution of the diffraction field from the 2D source $p(x,y) = C_1 \prod_{\alpha=x,y} \frac{p_0}{g_\alpha} \mathrm{comb}\left(\frac{\alpha}{g_\alpha}\right) \times \mathrm{rect}\left(\frac{\alpha}{L_\alpha}\right) * \mathrm{rect}\left(\frac{\alpha}{b_\alpha}\right)$, where $g_\alpha = 2.5\lambda$, $L_\alpha = 50\lambda$, and $b_\alpha = 1.5\lambda$. (b) The intensity distribution of the diffraction field from the 2D source $p(x,y) = C_1 \prod_{\alpha=x,y} \frac{p_0}{g_\alpha} \mathrm{comb}\left(\frac{\alpha}{g_\alpha}\right) \times \mathrm{rect}\left(\frac{\alpha}{L_\alpha}\right) * \mathrm{rect}\left(\frac{\alpha}{b_\alpha}\right)$, where $g_\alpha = 2.5\lambda$, $L_\alpha = 50\lambda$, and $b_\alpha = 2.5\lambda$. (c) The intensity distribution of the diffraction field from the 2D source $p(x,y) = C_1 \prod_{\alpha=x,y} \frac{p_0 e^{-\alpha^2/\tau_\alpha^2}}{g_\alpha} \mathrm{comb}\left(\frac{\alpha}{g_\alpha}\right) \times \mathrm{rect}\left(\frac{\alpha}{L_\alpha}\right) * \mathrm{rect}\left(\frac{\alpha}{b_\alpha}\right)$, where $g_\alpha = 2.5\lambda$, $L_\alpha = 50\lambda$, $b_\alpha = 2.5\lambda$, and $\tau_\alpha = 13\lambda$. (d) The schematic of the 2D active acoustic metasurface. (e) The photo of the packaged sample for medical applications.

piezoelectric sheets in a matrix of epoxy resin, as shown in Fig. 3(d), where the filling ratio of piezoelectric sheets in one supercell is about 0.51. The metasurface is sandwiched between a matching layer and a backing layer not only for waterproof and protection packaging, but also for the best coupling of ultrasound into water. The matching layer and the backing layer are made of aluminum oxide/epoxy resin and aluminum nitride/epoxy resin, respectively. The lab-made device sample is shown in Fig. 3(e).

In ultrasound focusing, it is necessary to introduce a phase distribution on the metasurface plane. Here, the phase distribution is realized by using programmable electric signals that control the vibrations of piezoelectric sheets. For the metasurface, the aperture function is

$$t(x,y) = \prod_{\alpha=x,y} \frac{1}{g_\alpha} \mathrm{comb}\left(\frac{\alpha}{g_\alpha}\right) \times \mathrm{rect}\left(\frac{\alpha}{L_\alpha}\right) * \mathrm{rect}\left(\frac{\alpha}{b_\alpha}\right),$$

where $g_\alpha = b_\alpha = 2.8$ mm and $L_\alpha = 44.8$ mm. The operation frequency is set at 1.04 MHz. The excitation function takes the form of $h(x,y) = A(x,y)e^{j\varphi(x,y)}$. Assume the focal spot locates at (ξ, η, z). The phase distribution on the metasurface is

$$\varphi(x,y) = k\sqrt{(\xi - x)^2 + (\eta - y)^2 + z^2}, \qquad (13)$$

where k denotes the wave number. Substituting $h(x,y)$ and $t(x,y)$ into Eq. (12), we will numerically obtain the radiation pattern of the active metasurface. For experiments, we conduct the measurements in a water tank ($400 \times 600 \times 1000$ mm^3). The active acoustic metasurface is driven by a Verasonics Vantage system with 256 channels. In order to eliminate the ultrasound echoes, we utilize a pulse series of 5-cycle square signals. The ultrasound field is scanned by a 0.5-mm-diameter needle hydrophone.
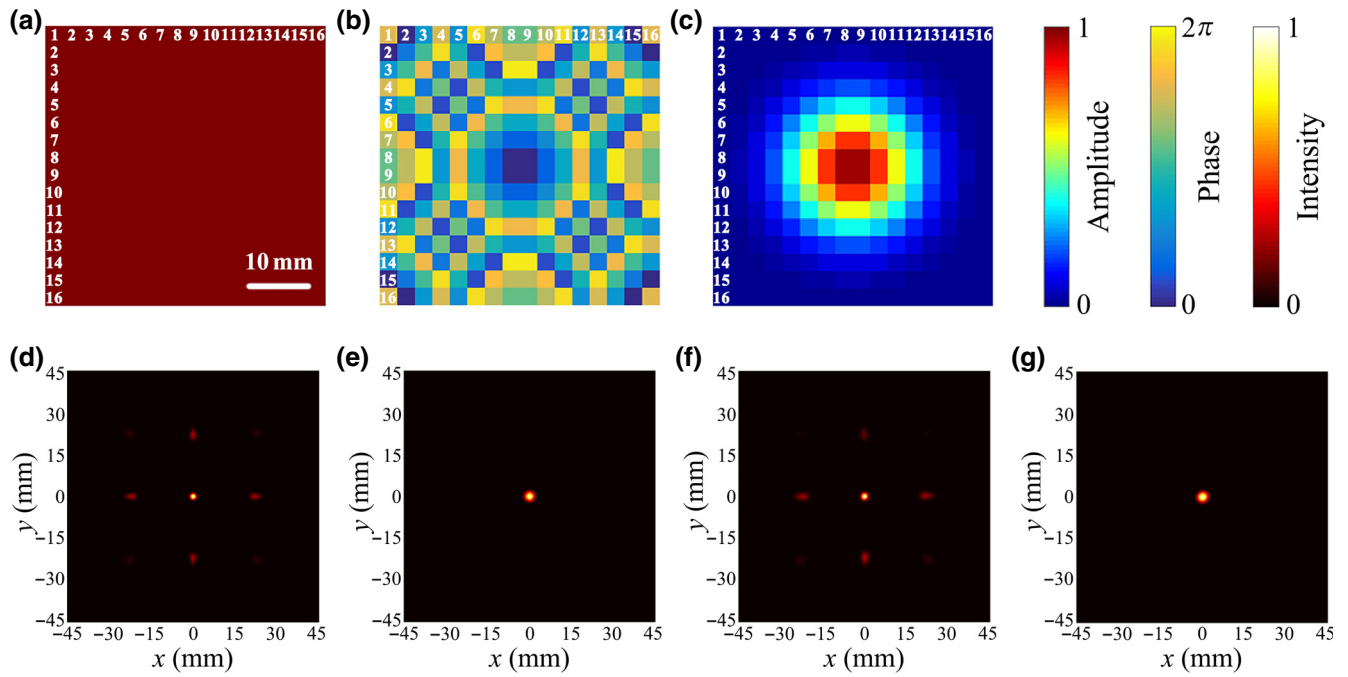
FIG. 4.   (a) The pressure amplitude distribution on the metasurface with $A(x,y) = p_0$. (b) The phase distribution with $\varphi(x,y) = k\sqrt{x^2 + y^2 + 40^2}$. (c) The amplitude distribution with $A(x,y) = p_0 e^{-(x^2+y^2)/\tau^2}$ and $\tau = 10$ mm. (d) The simulated intensity fields on the x-y plane with the amplitude and phase on the metasurface distributed as those in (a) and (b). (e) The simulated intensity fields on the x-y plane with the amplitude and phase on the metasurface distributed as those in (c) and (b). (f) The measured intensity fields on the x-y plane with the amplitude and phase on the metasurface distributed as those in (a) and (b). (g) The measured intensity fields on the x-y plane with the amplitude and phase on the metasurface distributed as those in (c) and (b).

All data are recorded with a digital storage oscilloscope (Agilent Technologies DSO-X-3034A) and processed by the Precision Acoustics UMS3 system software.

In Figs. 4(a)−4(g), we numerically and experimentally investigate the focusing functionality of the acoustic metasurface with the focal spot at (0, 0, 40) mm. In light of Eq. (13), the phase distribution is $\varphi(x,y) = k\sqrt{x^2 + y^2 + 40^2}$, as shown in Fig. 4(b). The amplitude modulation can be either homogenous ($A = p_0$) or Gaussian-shaped ($A =$ $p_0 e^{-(x^2+y^2)/\tau^2}$), as shown in Figs. 4(a) and 4(c), with $\tau = 10$ mm. When the amplitude on the metasurface is constant, new grating lobes are generated due to inhomogeneous phase distribution on the metasurface, as verified both numerically and experimentally in Figs. 4(d) and 4(f). To eliminate the grating lobes, we need to adopt Gaussian-shaped amplitude modulation, as also demonstrated numerically and experimentally in Figs. 4(e) and 4(g). The experimental result is in perfect agreement with
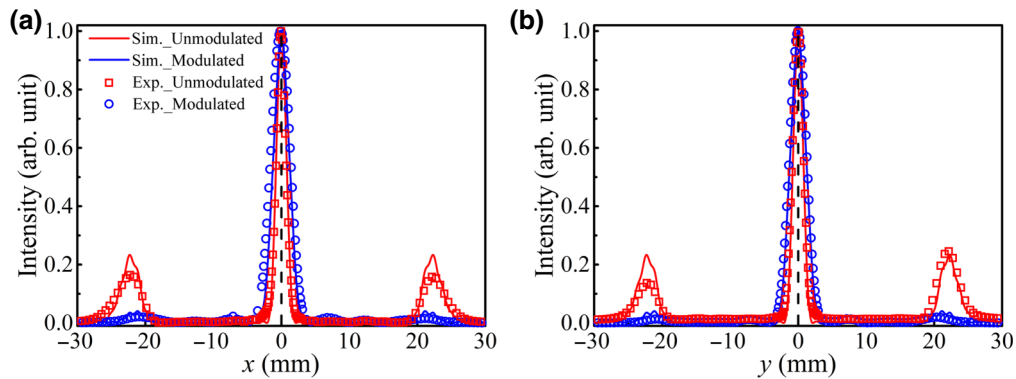

FIG. 5.   (a) The simulated and measured intensity distribution along the line $x = [-30, 30]$mm, $y = 0$ mm, $z = 40$ mm. (b) The simulated and measured intensity distribution along the line $x = 0$ mm, $y = [-30, 30]$mm, $z = 40$ mm.

the numerical simulation. A quantitative analysis is also given in Figs. 5(a) and 5(b), where we show the simulated and measured intensity distribution along the line $x = [-30, 30]$ mm, $y = 0$ mm, $z = 40$ mm and the line $x = 0$ mm, $y = [-30, 30]$ mm, $z = 40$ mm, respectively. In Fig. 5, the red curves and square dots denote the simulated and measured data for the case where the amplitude and phase on the metasurface are distributed as the ones in Figs. 4(a) and 4(b). The blue curves and circle dots denote the simulated and measured data for the case where the amplitude and phase on the metasurface are distributed as the ones in Figs. 4(c) and 4(b). The result shows that the elimination of grating lobes will not affect the location of the main lobe (the focal spot). However, the lobe size is slightly wider.

Figures 6(a)–6(g) further demonstrate the focus steering functionality of the active acoustic metasurface, where the focal spot is shifted to the point (10, 10, 40) mm. In this case, the phase distribution is $\varphi(x,y) = k\sqrt{(x-10)^2 + (y-10)^2 + 40^2}$, as shown in Fig. 6(b). The amplitude modulation is either homogenous ($A = p_0$) or Gaussian-shaped ($A = p_0 e^{-[(x-10)^2 + (y-10)^2]/\tau^2}$), as

shown in Figs. 6(a) and 6(c), respectively, with $\tau = 10$ mm. For a homogenous amplitude distribution on the metasurface, in the same way, new grating lobes are generated in the field of view, as shown numerically in Fig. 6(d) and experimentally in Fig. 6(f). To eliminate these grating lobes, we utilize the shifted Gaussian-shaped amplitude modulation, for which the results are demonstrated numerically in Fig. 6(e) and experimentally in Fig. 6(g). We also present a quantitative analysis in Figs. 7(a) and 7(b), where we show the simulated and measured intensity distribution along the line $x = [-30, 30]$ mm, $y = 10$ mm, $z = 40$ mm and the line $x = 10$ mm, $y = [-30, 30]$ mm, $z = 40$ mm, respectively. In Fig. 7, the red curves and square dots denote the simulated and measured data for the case where the amplitude and phase on the metasurface are distributed as those in Figs. 6(a) and 6(b). The blue curves and circle dots denote the simulated and measured data for the case where the amplitude and phase on the metasurface are distributed as those in Figs. 6(c) and 6(b). Similarly, in the focus steering process, the location of the main lobe (the focal spot) will not change at all before and after using the technique of grating-lobe elimination, but the main lobe will be slightly expanded.
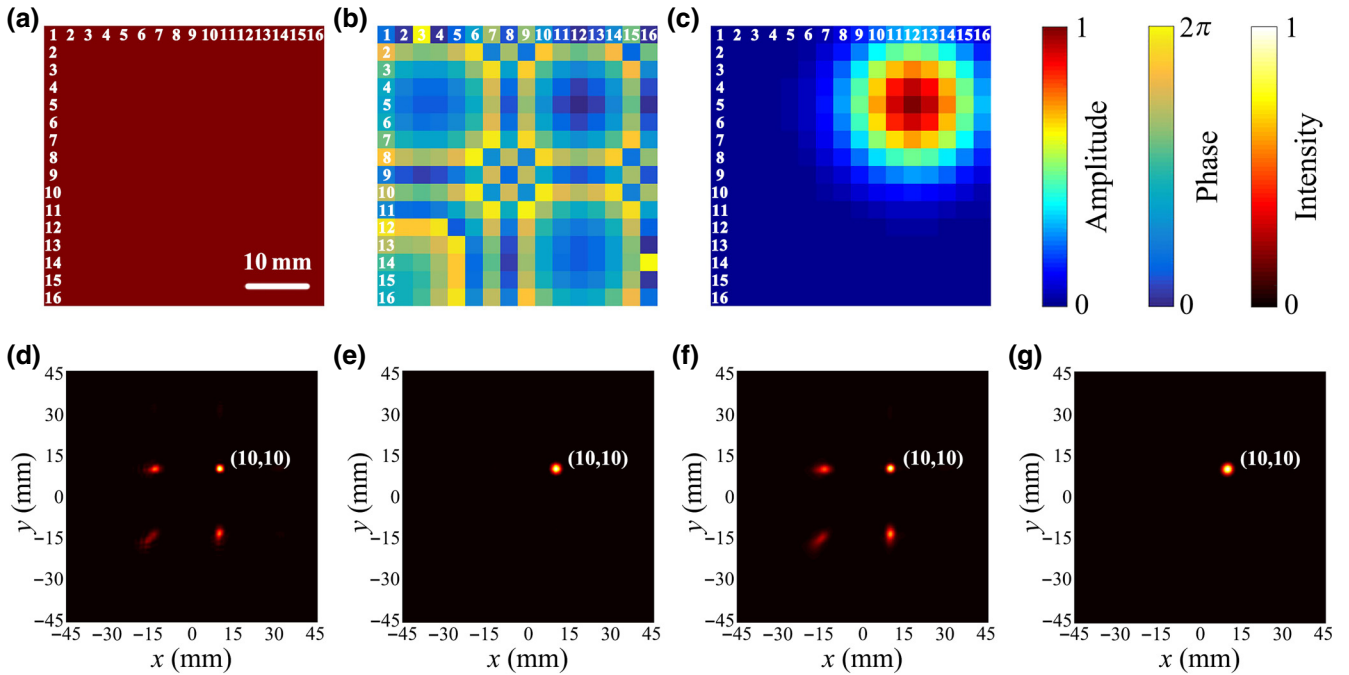

FIG. 6. (a) The pressure amplitude distribution with $A(x,y) = p_0$. (b) The phase distribution with $\varphi(x,y) = k\sqrt{(x-10)^2 + (y-10)^2 + 40^2}$. (c) The amplitude distribution with $A(x,y) = p_0 e^{-[(x-10)^2 + (y-10)^2]/\tau^2}$ and $\tau = 10$ mm. (d) The simulated intensity fields on the x-y plane with the amplitude and phase on the metasurface distributed as those in (a) and (b). (e) The simulated intensity fields on the x-y plane with the amplitude and phase on the metasurface distributed as those in (c) and (b). (f) The measured intensity fields on the x-y plane with the amplitude and phase on the metasurface distributed as those in (a) and (b). (g) The measured intensity fields on the x-y plane with the amplitude and phase on the metasurface distributed as those in (c) and (b). The operation frequency $f = 1.04$ MHz.
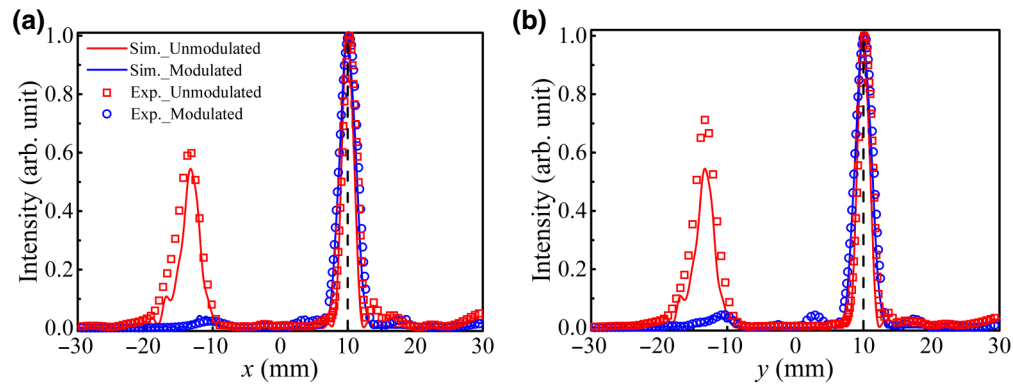
FIG. 7. (a) The simulated and measured intensity distribution along the line $x = [-30, 30]$ mm, $y = 10$ mm, $z = 40$ mm. (b) The simulated and measured intensity distribution along the line $x = 10$ mm, $y = [-30, 30]$mm, $z = 40$ mm.

IV. CONCLUSIONS

In conclusion, we implement an active acoustic meta-surface for ultrasound beam engineering. We choose an important application, steerable focusing, and investigate how to eliminate the grating lobes and side lobes to prevent off-target heating that is unwanted in medical treatment. The theoretical analysis shows that the generation of grating lobes is rooted in the diffraction from the finite-sized source array and the different phase delays of the phased array. Therefore, we propose a two-step approach to completely get rid of these lobes. We first make the active elements on the metasurface closely packed, where for the periodically arrayed elements, the lattice constant equals the element width. Due to the diffraction theory, the grating lobes in terms of the structure diffraction will be completely suppressed. Then we impose Gaussian-shaped amplitude modulation on the metasurface to wipe out the grating lobes induced by inhomogeneous phase delays as well as the side lobes (or speckles). Thanks to the powerful programmable electric drive, the active metasurface has tunable amplitude and phase modulations, which ensures freewheeling ultrasound focusing. In the steering process, the position of the focal spot will not change after using the technique of grating-lobe elimination. Our work paves the way for the active-metasurface-based devices in the ultrasonic regime and shows promising potentials in the fields of medical ultrasonics and underwater acoustics.

[1] C. Mougenot, M. O. Kohler, J. Enholm, B. Quesson, A. Partanen, C. Moonen, and G. J. Ehnholm, MR monitoring of the near-field HIFU heating, AIP Conf. Proc. **1113**, 159 (2009).

[2] C. Mougenot, M. O. Kohler, J. Enholm, B. Quesson, and C. Moonen, Quantification of near-field heating during volumetric MR-HIFU ablation, Med. Phys. **38**, 272 (2011).

[3] D. N. Stephens, D. E. Kruse, S. P. Qin, and K. W. Ferrara, Design aspects of focal beams from high-intensity arrays, IEEE Trans. Ultrason. Ferroelectr. Freq. Control **58**, 1590 (2011).

[4] M. Kohler, C. Mougenot, and M. Ylihautala, Near-field heating of volumetric MR-HIFU hyperthermia, AIP Conf. Proc. **1481**, 180 (2012).

[5] V. Chaplin, M. A. Phipps, and C. F. Caskey, A random phased-array for MR-guided transcranial ultrasound neuromodulation in non-human primates, Phys. Med. Biol. **63**, 105016 (2018).

[6] W. Legon, T. F. Sato, A. Opitz, J. Mueller, A. Barbour, A. Williams, and W. J. Tyler, Transcranial focused ultrasound modulates the activity of primary somatosensory cortex in humans, Nat. Neurosci. **17**, 322 (2014).

[7] D. M. Panczykowski, E. A. Monaco, and R. M. Friedlander, Transcranial focused ultrasound modulates the activity of primary somatosensory cortex in humans, Neurosurgery **74**, N8 (2014).

[8] W. J. Elias *et al.*, A randomized trial of focused ultrasound thalamotomy for essential tremor, New Engl. J. Med. **375**, 730 (2016).

[9] W. Lee, H. C. Kim, Y. J. Jung, Y. A. Chung, I. U. Song, J. H. Lee, and S. S. Yoo, Transcranial focused ultrasound stimulation of human primary visual cortex, Sci. Rep. **6**, 34026 (2016).

[10] H. Kim, A. Chiu, S. D. Lee, K. Fischer, and S. S. Yoo, Focused ultrasound-mediated non-invasive brain stimulation: Examination of sonication parameters, Brain Stimul. **7**, 748 (2014).

[11] R. L. King, J. R. Brown, and K. B. Pauly, Localization of ultrasound-induced in vivo neurostimulation in the mouse model, Ultrasound Med. Biol. **40,** 1512 (2014).

[12] W. Lee, Y. A. Chung, Y. J. Jung, I. U. Song, and S. S. Yoo, Simultaneous acoustic stimulation of human primary and secondary somatosensory cortices using transcranial focused ultrasound, BMC Neurosci. **17,** 68 (2016).

[13] J. P. Do-Huu and P. Hartemann, Annular array transducer for deep acoustic hyperthermia, Ultrasonics Symp. (IEEE) (1981), pp. 705.

[14] E. S. Ebbini and C. A. Cain, A spherical-section ultrasound phased array applicator for deep localized hyperthermia, IEEE Trans. Biomed. Eng. **38,** 634 (1991).

[15] L. R. Gavrilov and J. W. Hand, A theoretical assessment of the relative performance of spherical phased arrays for ultrasound surgery, IEEE Trans. Ultrasonics Ferroelectr. Freq. Control **47,** 125 (2000).

[16] J. Hand, A. Shaw, N. Sadhoo, S. Rajagopal, R. Dickinson, and L. Gavrilov, A random phased array device for delivery of high intensity focused ultrasound, Phys. Med. Biol. **54,** 5675 (2009).

[17] O. Martinez, C. J. Martin, G. Godoy, and L. G. Ullate, 2D array based on fermat spiral, Phys. Proc. **3,** 399 (2010).

[18] N. Ellens, A. Pulkkinen, J. Song, and K. Hynynen, The utility of sparse 2D fully electronically steerable focused ultrasound phased arrays for thermal surgery: a simulation study, Phys. Med. Biol. **56,** 4913 (2011).

[19] P. Ramaekers, M. D. Greef, R. Berriet, C. T. W. Moonen, and M. Ries, Evaluation of a novel therapeutic focused ultrasound transducer based on Fermat's spiral, Phys. Med. Biol. **62,** 5021 (2017).

[20] A. Hughes, Y. X. Huang, A. Pulkkinen, M. L. Schwartz, A. M. Lozano, and K. Hynynen, A numerical study on the oblique focus in MR-guided transcranial focused ultrasound, Phys. Med. Biol. **61,** 8025 (2016).

[21] Y. Li, B. Liang, X. Tao, X. F. Zhu, X. Y. Zou, and J. C. Cheng, Acoustic focusing by coiling up space, Appl. Phys. Lett. **101,** 233508 (2012).

[22] Y. Li, B. Liang, Z. M. Gu, X. Y. Zou, and J. C. Cheng, Reflected wavefront manipulation based on ultrathin planar acoustic metasurfaces, Sci. Rep. **3,** 2546 (2013).

[23] K. Tang, C. Y. Qiu, M. Z. Ke, J. Y. Lu, Y. T. Ye, and Z. Y. Liu, Anomalous refraction of airborne sound through ultrathin metasurfaces, Sci. Rep. **4,** 6517 (2014).

[24] Y. Li, X. Jiang, R. Q. Li, B. Liang, X. Y. Zou, L. L. Yin, and J. C. Cheng, Experimental Realization of Full Control of Reflected Waves with Subwavelength Acoustic Metasurfaces, Phys. Rev. Appl. **2,** 064002 (2014).

[25] Y. B. Xie, W. Q. Wang, H. Y. Chen, A. Konneker, B. Popa, and S. A. Cummer, Wavefront modulation and subwavelength diffractive acoustics with an acoustic metasurface, Nat. Commun. **5,** 5553 (2014).

[26] X. X. Wu, X. X. Xia, J. X. Tian, Z. Y. Liu, and W. J. Wen, Broadband reflective metasurface for focusing underwater ultrasonic waves with linearly tunable focal length, Appl. Phys. Lett. **108,** 163502 (2016).

[27] X. F. Zhu, K. Li, P. Zhang, J. Zhu, J. T. Zhang, C. Tian, and S. C. Liu, Implementation of dispersion-free slow acoustic wave propagation and phase engineering with helical-structured metamaterials, Nat. Commun. **7,** 11731 (2016).

[28] B. Y. Xie, K. Tang, H. Cheng, Z. Y. Liu, S. Q. Chen, and J. G. Tian, Coding Acoustic Metasurfaces, Adv. Mater. **29,** 1603507 (2017).

[29] H. C. Tang, Z. S. Chen, N. Tang, S. F. Li, Y. X. Shen, Y. G. Peng, X. F. Zhu, and J. F. Zang, Hollow-out patterning ultrathin acoustic metasurfaces for multifunctionalities using soft fiber/rigid bead networks, Adv. Funct. Mater. **28,** 1801127 (2018).

[30] Y. F. Zhu, J. Hu, X. D. Fan, J. Yang, B. Liang, X. F. Zhu, and J. C. Cheng, Fine manipulation of sound via lossy metamaterials with independent and arbitrary reflection amplitude and phase, Nat. Commun. **9,** 1632 (2018).

[31] B. Assouar, B. Liang, Y. Wu, Y. Li, J. C. Cheng, and Y. Jing, Acoustic metasurfaces, Nat. Rev. Mater. **3,** 460 (2018).

[32] G. C. Ma, X. Y. Fan, P. Sheng, and M. Fink, Shaping reverberating sound fields with an actively tunable metasurface, Proc. Natl. Acad. Sci. U.S.A. **115,** 6638 (2018).

[33] Y. F. Zhu, X. D. Fan, B. Ling, J. C. Cheng, and Y. Jing, Ultrathin Acoustic Metasurface-Based Schroeder Diffuser, Phys. Rev. X **7,** 021034 (2017).

[34] P. Zhang, T. C. Li, J. Zhu, X. F. Zhu, S. Yang, Y. Wang, X. B. Yin, and X. Zhang, Generation of acoustic self-bending and bottle beams by phase engineering, Nat. Commun. **5,** 4316 (2014).

[35] P. M. Morse and K. U. Ingard, *Theoretical Acoustics* (Princeton University Press, Princeton, 1987), 1st ed.

[36] M. Born and E. Wolf, *Principles of Optics: Electromagnetic Theory of Propagation, Interference and Diffraction of Light* (Cambridge University Press, Cambridge, 1999), Seventh (expanded) Edition.

[37] J. W. Goodman, *Introduction to Fourier Optics* (McGraw Hill Higher Education, New York, 1996), 2nd ed.